RSC Advances

PAPER

View Article Online
View Journal | View Issue

Cite this: *RSC Adv.*, 2017, **7**, 24255

Monodisperse, shape-selective synthesis of YF_3:Yb^{3+}/Er^{3+} nano/microcrystals and strong upconversion luminescence of hollow microcrystals†

G. Murali,[a] Sandeep Kaur,[a] Young Cheol Chae,[a] Manda Ramesh,[a] Jongwoo Kim,[b] Yung Doug Suh,[b] Dong-Kwon Lim *[c] and Seung Hee Lee*[a]

Received 21st February 2017
Accepted 27th April 2017

DOI: 10.1039/c7ra02188g

rsc.li/rsc-advances

Synthesizing upconversion materials with 3-dimensional structures is of fundamental importance in understanding the relationship between their optical properties and their structures. In this paper, we report a simple but useful synthetic method to produce highly monodisperse 3-dimensional YF_3:Yb^{3+}/Er^{3+} microcrystals showing variable upconversion efficiencies. By tuning the pH, precursor salt, and solvent, the shapes of the YF_3:Yb^{3+}/Er^{3+} crystals could be tuned from hollow hexagon to hollow dumbbell, tetragonal bipyramid, and truncated tetragonal bipyramid structures. The upconversion efficiency showed significant dependence on the structure of YF_3:Yb^{3+}/Er^{3+}; hollow structures revealed a large enhancement in the luminescence intensity. The upconversion efficiency of the structures decreased in the order hollow hexagon > hollow dumbbell > tetragonal bipyramid > truncated tetragonal bipyramid.

1. Introduction

Precise control over the shape and size of an inorganic functional material facilitates the manipulation of structural, optical, and magnetic properties as desired.[1–3] Shape-controlled synthesis of upconversion (UC) materials has long been the focus of intense research efforts in materials science and technology.[4–6] Because of their relatively low phonon energies and high chemical stability compared to hydroxides, oxides, phosphates, and vanadates, fluorides have been regarded as best host materials to yield high UC efficiency.[7] In particular, Yb^{3+} and Er^{3+} co-doped rare-earth fluorides have unique size- and shape-dependent UC emission properties that have stimulated intensive investigation into their possible applications in various fields during the last decade.[7–10] Wet chemical synthetic strategies, especially hydro/solvothermal and thermal decomposition methods, have been demonstrated to be efficient and expedient in preparing highly crystalline rare-earth fluorides with diverse tunable morphologies.[7,8] However, these methods have typically required the use of an appropriate organic surfactant to generate the preferred crystal shape by controlling the crystal growth rate along certain crystallographic axes during the nucleation stage.[7,8] The binding characteristics of these organic surfactants over the surface leads to an unwanted surface contamination that diminishes the UC efficiency. Furthermore, complex reaction procedures are required to either replace or remove the surfactant to make UC morphologies suitable for their specified applications.[7,8] Therefore, it is necessary to design a synthetic strategy to generate more advanced rare-earth fluoride shapes with high UC efficiency, without using organic surfactants.

Among various rare-earth fluorides, YF_3 is best-known for its high UC efficiency[11–15] and has potential applications in various fields such as solid-state lasers,[16] solar cells,[17,18] photocatalysis,[19,20] and the life sciences.[21] Lately, enhancing the luminescence efficiency of YF_3 has been the challenging task.[21–23] The structure and crystalline phase of YF_3 has been found to have a significant control over its emissive performance.[24–26] So far, several YF_3 nano- and microstructures have been synthesized using a variety of methods to investigate their unprecedented shape- and size-dependent up/down-conversion emission properties.[21–29] A majority of the adopted synthetic methods require organic surfactants to control the structure. Shao *et al.*[30] reported a simple surfactant-free HNO_3-assisted hydrothermal method to finely tune the structure of YF_3:Eu^{3+} to generate various shapes. They observed increased luminescence

[a]*Applied Materials Institute for BIN Convergence, Department of BIN Convergence Technology, Department of Polymer-Nano Science and Technology, Chonbuk National University, Jeonju, Jeonbuk 561-756, Korea. E-mail: lsh1@chonbuk.ac.kr; Tel: +82-63-270-2343*

[b]*Laboratory for Advanced Molecular Probing (LAMP), Korea Research Institute of Chemical Technology, Daejeon 305-600, South Korea*

[c]*KU-KIST Graduate School of Converging Science and Technology, Korea University, 145 Anam-ro, Seongbuk-gu, Seoul 136-701, Korea. E-mail: dklim@korea.ac.kr*

† Electronic supplementary information (ESI) available. See DOI: 10.1039/c7ra02188g

intensities when the particle shape changed from diamond to octahedral and finally to truncated octahedral. Zhang *et al.*[31] reported the phase transformation from orthorhombic phase YF_3:Yb^{3+}/Er^{3+} to tetragonal phase $LiYF_4$:Yb^{3+}/Er^{3+}, and sharp increase in UC luminescence intensity was found with increasing pH of the mother solution. We also recently found a synthetic method for producing nanoplate structures of YF_3:Yb^{3+}/Er^{3+} nanocrystals with strong luminescent properties by controlling the concentration of NaOH.[32]

Herein, we report a simple hydrothermal method that can produce highly monodisperse 3-dimensional (3D) structures of YF_3:Yb^{3+}/Er^{3+} by changing the reaction parameters, including precursor salt type, pH of the initial solution, and solvent composition. The 3D hollow hexagon shows the highest UC luminescence properties compared with the hollow dumbbell, tetragonal bipyramid, and truncated tetragonal bipyramid structures prepared in this study.

2. Experimental

2.1 Materials

$Y(NO_3)_3 \cdot 6H_2O$, $Yb(NO_3)_3 \cdot 5H_2O$, $Er(NO_3)_3 \cdot 5H_2O$, $YCl_3 \cdot 6H_2O$, $YbCl_3 \cdot 6H_2O$, $ErCl_3 \cdot 6H_2O$, NH_4F, and KF were purchased from Sigma-Aldrich (St. Louis, MO, USA). NaF was supplied by Daejung Chemicals & Metals Co., Ltd (Siheung-si, Gyeonggi-do, Korea). All chemicals were used as received without further purification.

2.2 Typical synthetic procedures for YF_3:Yb^{3+}/Er^{3+} structures

In a typical procedure, 1.56 mmol $Y(NO_3)_3 \cdot 6H_2O$, 0.4 mmol $Yb(NO_3)_3 \cdot 5H_2O$, and 0.04 mmol $Er(NO_3)_3 \cdot 5H_2O$ were dissolved in 70 mL deionized water, then 6 mmol of NH_4F was added under vigorous stirring at room temperature. The pH of the mixed solution was adjusted with the addition of HNO_3 (28%) or NaOH (2.5 M). The resulting solution was transferred into a Teflon autoclave with an 80 mL capacity. The autoclave was maintained at 160 °C for 16 h, and then air-cooled to room temperature naturally. Then, the white precipitate was separated *via* centrifugation (5000 rpm/10 min) and washed with ethanol and distilled water several times. Finally, the precipitate was dried in air at 80 °C for 8 h. The effect of the precursor salt type on the resulting YF_3:Yb^{3+}/Er^{3+} structure was investigated by using rare-earth nitrate and rare-earth chlorides, along with NH_4F, KF, and NaF as the fluoride source, without otherwise altering the reaction conditions.

2.3 Characterization

The crystallinity of the nanostructures was determined by X-ray powder diffraction (XRD, MAX-2500, Rigaku) using Fe-filtered Cu-K_α radiation (λ = 1.54 Å). The products were characterized by high-resolution transmission electron microscopy (HRTEM, H-7650, Hitachi and JEM-2010, Jeol) and field emission scanning electron microscopy (FESEM; SU-70, Hitachi).

3. Results and discussion

A variety of YF_3:Yb^{3+}/Er^{3+} microcrystals were synthesized *via* hydrothermal reaction of rare-earth nitrate or chloride precursors in the presence of NH_4F, NaF, and KF. Particle size and shape are readily controlled by adjusting the pH of the initial solution.

3.1 Morphology control with rare-earth nitrate precursors (pH 1.2)

In a typical synthesis, rare-earth (RE) nitrate precursors and NH_4F (F^-/RE^{3+} ratio = 3.0) were used, with the pH adjusted to 1.2. The SEM images of the as-prepared YF_3:Yb^{3+}/Er^{3+} sample are shown in Fig. 1a–d. Fig. 1a indicate the formation of a large quantity of uniform dumbbell-shaped particles. A close-up view reveals that the dumbbell-shaped structures possess large isosceles triangle-shaped heads separated by a comparatively small shaft (Fig. 1b). The end to end distance of the dumbbell is about 1.46 μm, while the shaft length is about 170 nm (Fig. 1b). The base and sides of the triangular heads are about 680 nm and 1.1 μm, respectively (Fig. 1b). Although the surface of the structure is smooth, the edges are not sharp. Furthermore, one can notice that these dumbbells are hollow in nature (Fig. 1c and S1†). The elemental mapping images for Y, F, Yb, and Er of dumbbell-shaped particles (Fig. 1d) demonstrates that the three elements of Y, F, and Yb are uniformly distributed throughout the dumbbell-like particles, while the element Er is not clearly evident because of its low concentration (Fig. 1e–h). This confirms that the formation of dumbbell-shaped structures is regular and not a result of any elemental segregation or accumulation. It is worth mentioning that, the pH value is critical in achieving the dumbbell shape morphology, the change in pH value on either side of 1.2 produces different morphologies (Fig. S2†).

We further examined the YF_3:Yb^{3+}/Er^{3+} dumbbell using TEM and HRTEM to investigate the detailed nanostructure (Fig. 1i–k). As shown in Fig. 1j, the clear contrast between the outer (dark) and inner (bright) parts of the dumbbell-shape further confirms the formation of a hollow dumbbell structure. The HRTEM shows well-defined lattice fringes separated by 70° with fringe spacing of 0.36 nm, which can be assigned to the (101) and ($\bar{1}$01) planes of orthorhombic YF_3 (Fig. 1k). The corresponding dot selected area electron diffraction (SAED) pattern reveals the single crystalline characteristic of the YF_3:Yb^{3+}/Er^{3+} dumbbells (Fig. 1l).

To determine the effect of fluoride source on these dumbbell-shaped structures, NH_4F was replaced with NaF or KF (Fig. 1m–p). It is very clear from the SEM images that the nature of the fluoride source affects the structure of the YF_3:Yb^{3+}/Er^{3+} microcrystals (Fig. 1m–p). Formation of rod-shaped clusters with small rice grain nanoparticles, which resembles a mosaic virus shape, is observed in the case of the NaF fluoride source, as shown in Fig. 1m and n. The diameter and length of the cluster are in the range of 300–500 nm and 800 nm to 1.2 μm, respectively (Fig. 1n). The presence of rice grain-like nanoparticles and the observation of rough particle surfaces in the

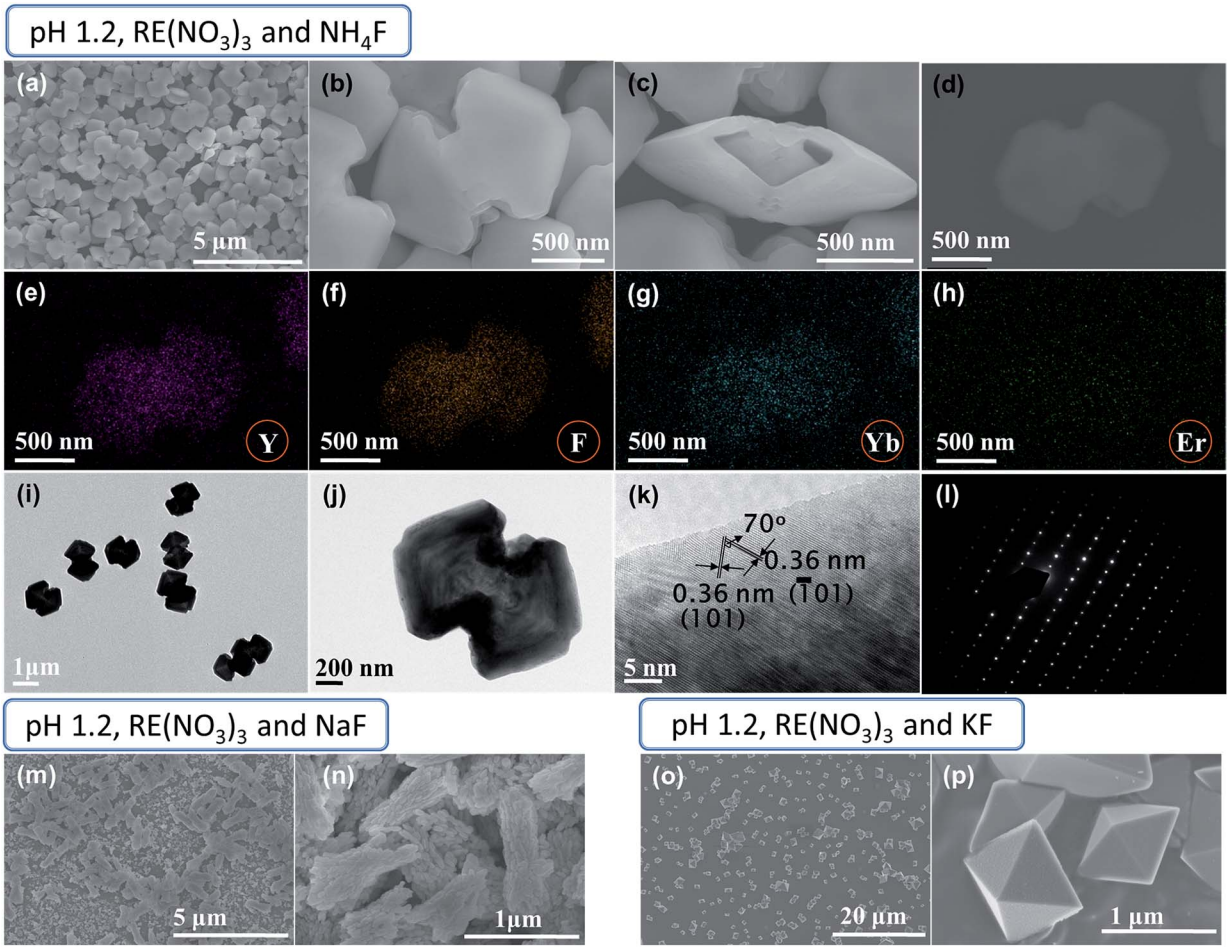

Fig. 1 (a–d) SEM images of YF_3:Yb^{3+}/Er^{3+} with dumbbell-shape morphology. (e–h) Elemental mapping for Y, F, Yb, and Er for the particle shown in (d). (i and j) TEM, (k) HRTEM, and (l) SAED pattern of dumbbell-shaped particles. SEM images of samples prepared with (m and n) NaF and (o and p) KF, at the same reaction conditions used to synthesize the dumbbell-shaped particles. Rare-earth nitrate precursors (*i.e.*, $RE(NO_3)_3$, where RE = Y, Yb, and Er were used, pH = 1.2), and the F^-/RE^{3+} ratio was 3.0.

close-up examination of the rod-shaped clusters suggests the construction of clusters occurs through ordered aggregation of many small primary rice grains-like nanoparticles (Fig. S3a and b†). The length and diameter of the rice grain-like nanoparticles are in the range of 50–180 nm and 35–100 nm, respectively (Fig. S3a†). When the NH_4F fluoride source was replaced by KF, the resulting YF_3:Yb^{3+}/Er^{3+} product consists exclusively of uniform and well-dispersed tetragonal bipyramidal-like structures (Fig. 1o and p). These have sharp edges with smooth triangular surfaces, and the edge length is in the range of 450 nm to 2.5 μm (Fig. 1o and p).

The XRD patterns of the as-synthesized products at pH 1.2 using different fluoride sources are shown in Fig. 2. The sharp diffraction peaks correspond to orthorhombic phase YF_3 (JCPDS no. 74-0911), confirming the high crystallinity of the samples. It is worth mentioning that the relative intensities of (101), (020), and (111) in the XRD patterns varied according to the structure of the particles, indicating that the morphologies possess different crystalline planes as their dominant surfaces.

3.2 Morphology control with rare-earth nitrate precursors (pH ≥ 2.0)

The increase in pH to 2.0 only resulted in the aggregation of submicrometer-sized particles to form spindle-like structures with lengths of *ca.* 700 nm to 1 μm and diameters of *ca.* 330–380 nm (Fig. 3a). For pH 3.0, a nanodisk structure is obtained (Fig. S4a†). Detailed observation indicates the disks have holes and a nut-like appearance (Fig. 3b). While at pH 4.0, the structures have a crystal layer grown perpendicular to the planar surface of the disks (Fig. S4b† and 3c). The diameters of the disks are in the range of *ca.* 400–600 nm (Fig. 3b and c). At pH 5.0, a dumbbell-shaped structure with a slightly disordered shape is obtained, while at pH 6.0, rod-shaped cluster structures are observed (Fig. 3d and e). The increase in pH to 8.0 resulted in the fusion of small particles to construct a rod-shaped structure (Fig. 3f). These structures converted to irregular slabs at pH 10.0 and finally nanometer-sized particles at pH 12.0 (Fig. 3g and h).

XRD patterns of as-prepared products at pH values from 2.0 to 12.0 are shown in Fig. 4. The structures prepared below pH

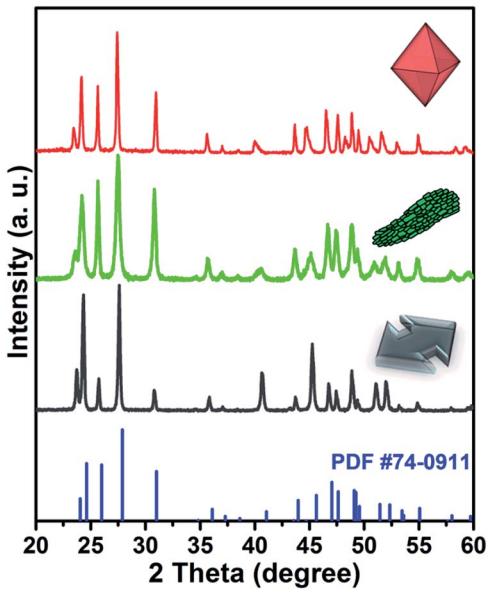

Fig. 2 XRD patterns of YF_3:Yb^{3+}/Er^{3+} structures prepared at pH = 1.2 with three different fluoride sources (NH_4F, NaF, and KF).

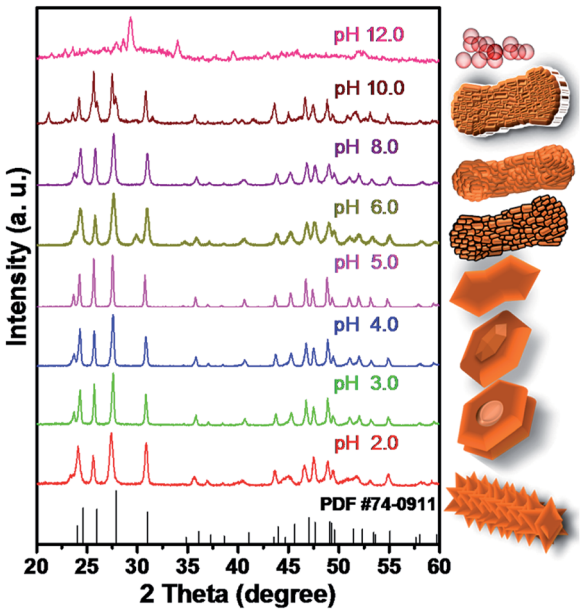

Fig. 4 XRD patterns of as-synthesized structures at different pH values (rare-earth nitrates and NH_4F were used as precursors).

10.0 display a pure orthorhombic YF_3 phase. The phase transformation from orthorhombic YF_3 to cubic $NaYF_4$ is observed for the sample prepared at pH 12.0. At this pH, a large amount of Na^+ ions released from the added NaOH (pH controlling agent) is introduced into the YF_3 crystal structure, which misbalances the orthorhombic YF_3 phase and induces the transformation from orthorhombic YF_3 to cubic $NaYF_4$ (Fig. 4 and S5†).

3.3 Morphology control with rare-earth chloride precursors

In addition to the above YF_3:Yb^{3+}/Er^{3+} structures, we could also control the morphology to give YF_3:Yb^{3+}/Er^{3+} hexagons and truncated tetragonal bipyramids, by using rare-earth chloride precursors instead of nitrates, changing the solvent composition, and varying the pH of the initial solution from 1.0 to 2.5.

Fig. 5 presents the morphological evolution of YF_3:Yb^{3+}/Er^{3+} samples prepared with increasing pH for the molar ratio F^-/RE^{3+} = 3.0. SEM analysis reveals that irregular micrometer-sized particles are formed at pH 1.0 (Fig. 5a). When the pH value increased to 1.5, elliptical-shaped aggregated particles are observed (Fig. 5b), with sizes in the range of 500 nm to 1 μm. At pH 2.0, monodisperse hexagon-shaped microcrystals are observed (Fig. 5c and d). The hexagons are extended along one axis, having a length around 350–400 nm, while the shorter sides are in the range of 250–350 nm (Fig. 5d). The tip-to-tip

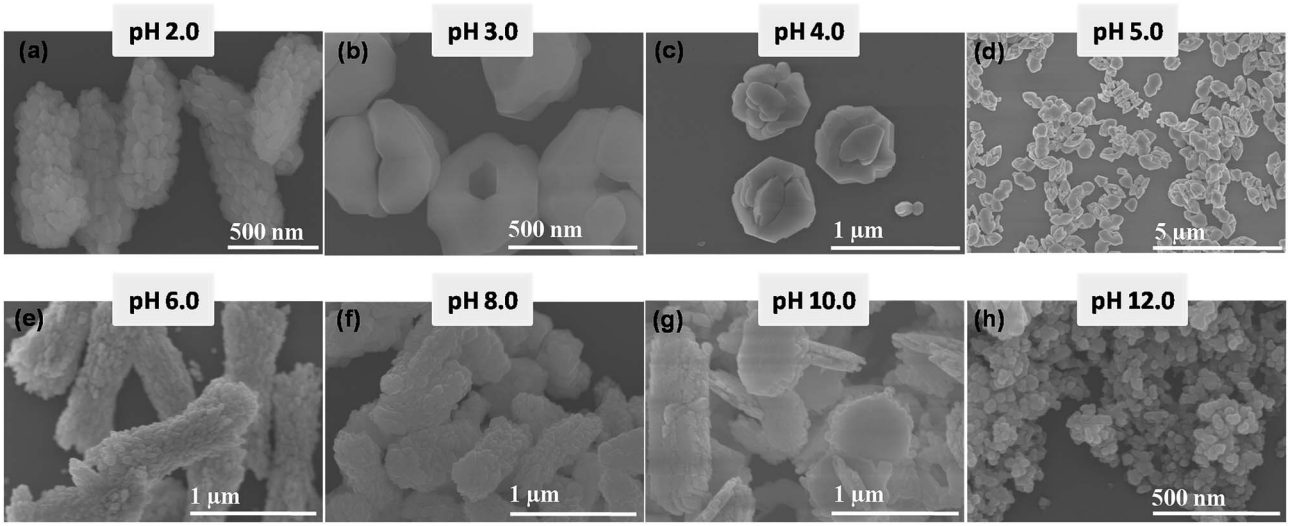

Fig. 3 SEM images of YF_3:Yb^{3+}/Er^{3+} samples prepared at pH values of (a) 2.0, (b) 3.0, (c) 4.0, (d) 5.0, (e) 6.0, (f) 8.0, (g) 10.0, and (h) 12.0 (rare-earth nitrates and NH_4F were used as precursors).

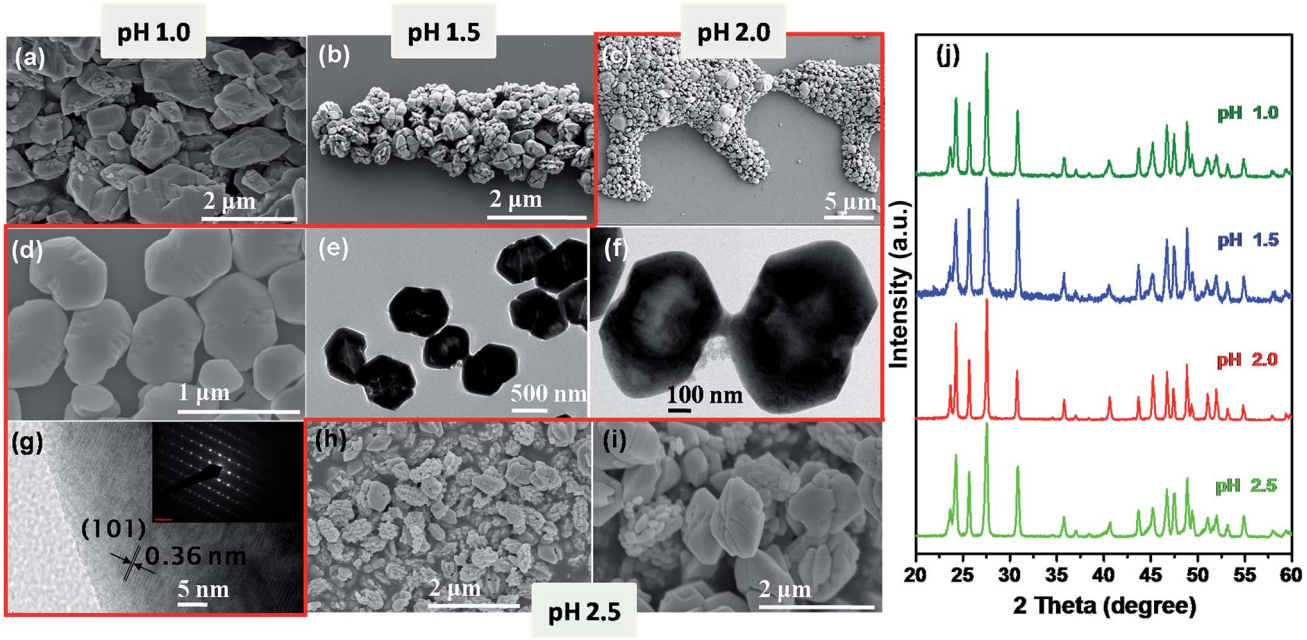

Fig. 5 SEM images of YF_3:Yb^{3+}/Er^{3+} samples prepared at pH values of (a) 1.0, (b) 1.5, (c and d), and 2.0. (e and f) TEM and (g) HRTEM (inset: SAED pattern) of elongated hexagon structure (pH 2.0). (h and i) SEM image of the sample prepared at pH 2.5. (j) XRD patterns of as-prepared structures (rare-earth chlorides and NH_4F were used as precursors).

distances of these structures are approximately 700 nm (Fig. 5d). Careful observation of the structure reveals that these hexagon-shaped particles actually possess hollow interiors (Fig. S6†). Regarding the TEM images of the hexagons (Fig. 5e and f), the contrast between the outer edges (dark) and the central parts (bright) further demonstrates their hollow nature. HRTEM of the hexagons revealed lattice planes with interplanar spacing of 0.36 nm that can be ascribed to the (101) plane of orthorhombic YF_3 (Fig. 5g). The symmetric SAED pattern shown in the inset of Fig. 5g indicates the single crystalline state of the hexagon-shaped particles. These elongated hexagons are distorted with the increase in pH from 2.0 to 2.5. As shown in Fig. 5h and i, misshapen hexagons along with aggregated particles are formed at pH 2.5.

Fig. 5j shows the XRD patterns of as-obtained samples with four typical morphologies, including irregular microparticles, elliptical-shaped aggregates, hexagons, and a mixture of hexagons and aggregated particle. According to JCPDS no. 74-0911, all the diffraction peaks coincide with the orthorhombic phase YF_3, without other impurity peaks.

3.4 Synthesis of highly monodisperse tetragonal bipyramid and truncated tetragonal bipyramid structures

The morphology of the particles is also tuned by changing the F^-/RE^{3+} molar ratio and solvent composition under the same reaction conditions at pH 1.5. Fig. 6a and b shows SEM images of the samples prepared with F^-/RE^{3+} ratios of 5.0 and 8.0. In both cases, well-defined tetragonal bipyramid structures are observed. However, tetragonal bipyramids are found to be interpenetrated at the higher F^-/RE^{3+} ratio (Fig. 6b). Additionally, changing the solvent from water to a mixture of water, ethanol, and methanol in a 4 : 2 : 1 ratio at pH 1.5 (F^-/RE^{3+} = 4.6), resulted in a morphological transformation from the tetragonal bipyramid structure to the uniform truncated tetragonal bipyramid structure (Fig. 6c). A close-up observation of these particles reveals a smooth surface and sharp edges (Fig. 6c). Their XRD patterns, shown in Fig. 6d, indicate the change in precursor composition and solvent did not result in any impurity phase in the predominantly orthorhombic YF_3 structure. Moreover, this indicates the importance of solvent and F^-/RE^{3+} alongside the pH value in controlling the YF_3:Yb^{3+}/Er^{3+} structure.

3.5 Photoluminescence properties

Fig. 7 shows the UC photoluminescence (PL) spectra of the as-prepared YF_3:Yb^{3+}/Er^{3+} structures (hollow dumbbell, hollow hexagon, tetragonal bipyramid, and truncated tetragonal bipyramid) at room temperature under the excitation of a 980 nm laser. All morphologies of YF_3:Yb^{3+}/Er^{3+} exhibit similar spectral patterns. The red emission band (640–685 nm) predominates over the green emission (535–560 nm), which are attributed to the $^4F_{9/2} \rightarrow {}^4I_{15/2}$ and $^4S_{3/2} \rightarrow {}^4I_{15/2}$ transitions, respectively (Fig. 7).[30] It is noteworthy that the green emission band consists of eight sub-bands, while the red emission band is made up of nine sub-bands. These sub-bands originate from the energy level splitting of the Er^{3+} ion in an orthorhombic YF_3 crystal field, confirming the Yb^{3+} and Er^{3+} dopant ions occupy the Y^{3+} sites with C_s symmetry in the YF_3 crystal lattice.[30,33–35]

It is interesting to note that, as shown in Fig. 7, the UC intensity varies notably with the shape of the YF_3:Yb^{3+}/Er^{3+} structure. The red emission shows a much larger variation in intensity than the green emission. The hollow hexagon

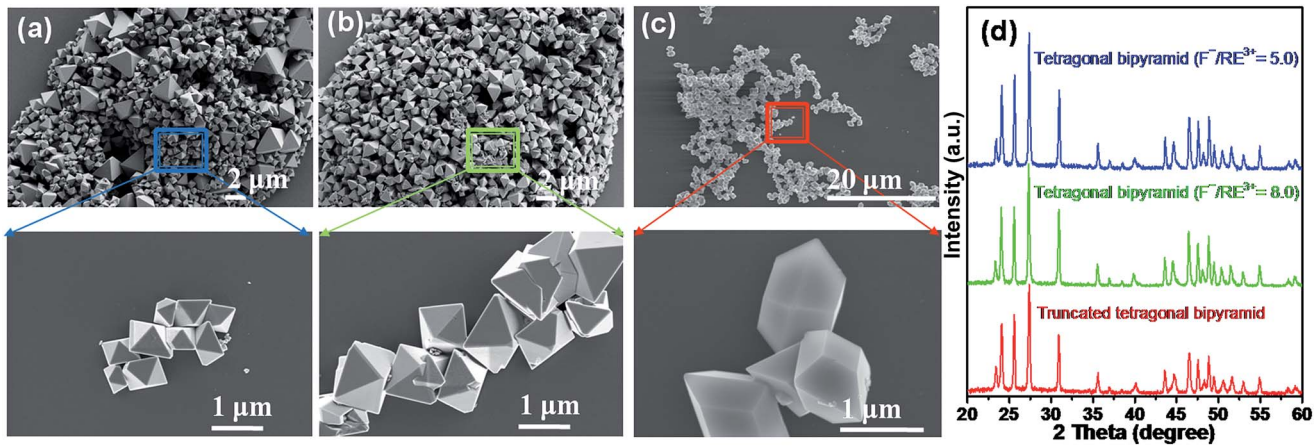

Fig. 6 SEM images of YF_3:Yb^{3+}/Er^{3+} samples prepared at pH 1.5 (a) $F^-/Re^{3+} = 5.0$, (b) $F^-/Re^{3+} = 8.0$ and (c) solvent composition: 4 : 2 : 1 ratio of water, ethanol and methanol and $F^-/Re^{3+} = 4.6$. (d) XRD patterns of as-prepared structures (rare-earth chlorides and NH_4F were used as precursors).

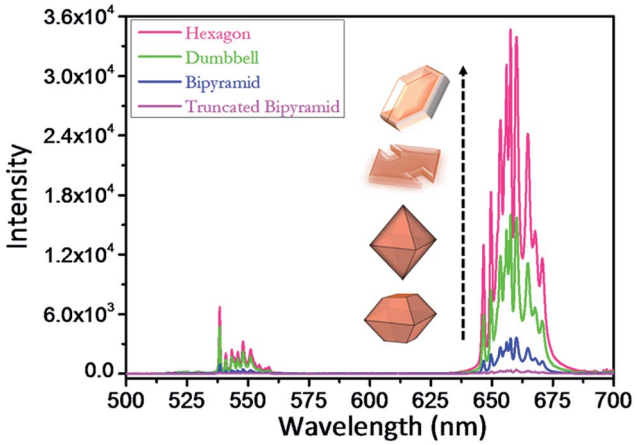

Fig. 7 Photoluminescence spectra of hollow hexagon, hollow dumbbell, tetragonal bipyramid, and truncated tetragonal bipyramid YF_3:Yb^{3+}/Er^{3+} microcrystals (1 mg ml^{-1}) excited with a 980 nm laser at 30 mW.

structure exhibits the strongest emission, the hollow dumbbell and tetragonal bipyramidal morphologies take second and third place, respectively, and the truncated tetragonal bipyramid exhibits the weakest emission. The integrated green and red PL intensity of the hollow hexagon structure is 77, 9, and 2 times higher than that of the truncated tetragonal bipyramid, tetragonal bipyramid, and dumbbell structures, respectively. The difference in UC intensity could be attributed to the shape of the structure and its defects. In general, defect formation occurs more at edges formed by the intersection of various crystal facets compared to any other location in the crystal.[30] Accordingly, the tetragonal bipyramidal and truncated tetragonal bipyramidal structures, which have many sharp edges, displayed poor emission properties compared to the hollow dumbbell and hexagon structures. Further, these hexagon and dumbbell structures have high surface areas compared to the other structures as they are hollow in nature. As the high surface area enhances the pumping photons absorption efficiency, the UC PL intensity is increased dramatically for these two structures.[36]

To demonstrate the precise influence of F^-/RE^{3+} ion concentration on the PL of the structures, we measured the PL of tetragonal bipyramids synthesized at two different F^-/RE^{3+} ratios of 5 and 8 (Fig. S7†). Only a slight decrease in intensity with increasing F^-/RE^{3+} ratio was seen (Fig. S7†), which might be due to the increased defect density due to the interpenetration of tetragonal bipyramids at higher F^-/RE^{3+} ratios (Fig. 6b). This confirms that the PL property largely depends on the shape and defect density associated with the structure.

3.6 The growth mechanism

Generally, during the crystal growth, the relative growth rate of seed crystal facets determines the shape of a resulting nano/microcrystal.[37] In the present investigation, distinct morphologies at various synthesis conditions (shown in Fig. 8) demonstrates the influence of synthetic parameters such as precursor salt type, pH of the initial solution and solvent composition on the resulting crystal structures. Under the fixed reaction conditions at pH = 1.2, rare earth precursor ($RE(NO_3)_3$) composition, reaction temperature at 160 °C and reaction time (16 h), the use of only different fluoride sources (*i.e.*, NH_4F, NaF and KF) resulted in significantly different particle structures. This indicates that the cations (NH_4^+, Na^+ and K^+) released from the fluoride source are participating in the growth process. Because of their strong interaction with the F^- anions, these ions selectively adsorb onto various crystal facets of seed YF_3 and these can induce the altered growth rate.[38] Due to the different cation size of NH_4^+, Na^+ and K^+ ions, the adsorption property of cations onto the crystal facets varies and leads to the formation of particles with different shapes.[38] It is reasonable to assume a similar situation for the ions released from pH controlling agents and rear earth precursor salts.[30] Even the use of ammonium fluoride (NH_4F) as a fluoride source, the change of pH can induce the different adsorption behavior of NH_4^+ ions onto the crystal facets and consequently leading to the

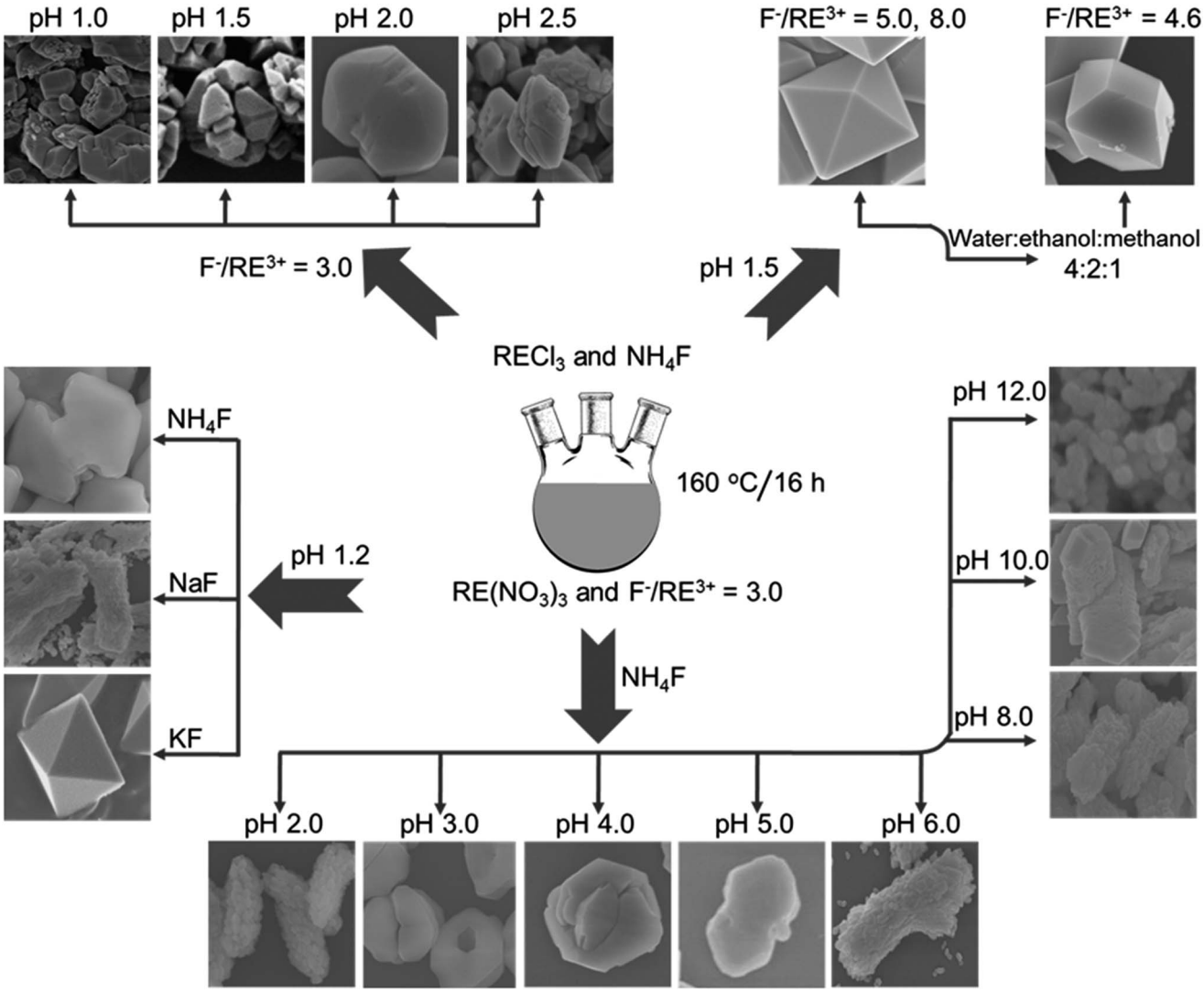

Fig. 8 Schematic illustration of the formation of YF_3:Yb^{3+}/Er^{3+} nano/microcrystals with various morphologies under different experimental conditions.

significant changes in morphology.[38] Furthermore, at higher concentrations, these ions attached to the facets can enter into the crystal lattice and distort the crystal symmetry.[32] Hence, for the samples prepared at pH = 12.0, Na^+ ion released from the added base (NaOH) to maintain basic pH enters into the YF_3 crystal lattice and causes the structural transformation from YF_3 to $NaYF_4$. Therefore, the diversity of morphology is due to the combined influence of pH value and precursor salts.

4. Conclusions

In summary, we demonstrated a simple hydrothermal method to produce well-defined 3D YF_3:Yb^{3+}/Er^{3+} nano/microcrystal structures by changing the reaction parameters. Precursor salt type and composition, solvent, and initial solution pH play critical roles in determining the final structures and monodispersity of YF_3:Yb^{3+}/Er^{3+}. The hollow hexagon, hollow dumbbell, tetragonal bipyramid, and truncated tetragonal bipyramid structures were obtained in a high yield. In particular, the hollow hexagon structure exhibited the strongest UC efficiency. Its strong luminescence can be attributed to the improved absorption ability of the hollow structures. With their improved UC efficiency, these hollow structures provide new opportunities for applications in photocatalysis, energy harvesting, and bioanalysis.

Acknowledgements

This research was supported by the National Research Foundation of Korea (NRF) funded by the Ministry of Education (NRF-2016R1A2B3013825), KU-KIST school project. This research was also supported by "Research Base Construction Fund Support Program" funded by Chonbuk National University in 2017.

Notes and references

1 T. P. Nguyen, W. Sohn, J. H. Oh, H. W. Jang and S. Y. Kim, *J. Phys. Chem. C*, 2016, **120**, 10078–10085.
2 G. Murali, D. A. Reddy, S. Sambasivam, G. Giribabu, R. P. Vijayalakshmi, R. Venugopal and B. K. Reddy, *Mater. Lett.*, 2013, **93**, 149–152.
3 G. Murali, D. A. Reddy, G. Giribabu, R. P. Vijayalakshmi and R. Venugopal, *J. Alloys Compd.*, 2013, **581**, 849–855.
4 Y. Liu, D. Tu, H. Zhuab and X. Chen, *Chem. Soc. Rev.*, 2013, **42**, 6924–6958.
5 T. Paik, A. M. Chacko, J. L. Mikitsh, J. S. Friedberg, D. A. Pryma and C. B. Murray, *ACS Nano*, 2015, **9**(9), 8718–8728.
6 T. Paik and C. B. Murray, *Nano Lett.*, 2013, **13**, 2952–2956.
7 G. Chen, H. Qiu, P. N. Prasad and X. Chen, *Chem. Rev.*, 2014, **114**, 5161–5214.
8 S. Gai, C. Li, P. Yang and J. Lin, *Chem. Rev.*, 2014, **114**(4), 2343–2389.
9 H. Na, K. Woo, K. Lim and H. S. Jang, *Nanoscale*, 2013, **5**, 4242–4251.
10 D. Yuan, M. C. Tan, R. E. Riman and G. M. Chow, *J. Phys. Chem. C*, 2013, **117**, 13297–13304.
11 F. Auzel and D. Pecile, *J. Lumin.*, 1976, **11**, 321–330.
12 F. Auzel and D. Pecile, *J. Lumin.*, 1973, **8**, 32–43.
13 F. Auzel, *Chem. Rev.*, 2004, **104**, 139–173.
14 G. Chen, H. Qiu, R. Fan, S. Hao, S. Tan, C. Yang and G. Han, *J. Mater. Chem.*, 2012, **22**, 20190–20196.
15 G. Wang, Q. Peng and Y. Li, *J. Am. Chem. Soc.*, 2009, **131**, 14200–14201.
16 A. Kaminskii, *Laser Crystals*, Springer, Berlin, 1990.
17 J. M. Meijer, L. Aarts, B. M. van der Ende, T. J. H. Vlugt and A. Meijerink, *Phys. Rev. B: Condens. Matter Mater. Phys.*, 2010, **81**, 035107.
18 J. Wu, J. Wang, J. Lin, Y. Xiao, G. Yue, M. Huang, Z. Lan, Y. Huang, L. Fan, S. Yin and T. Sato, *Sci. Rep.*, 2013, **3**, 2058.
19 Z. Li, C. Li, Y. Mei, L. Wang, G. Du and Y. Xiong, *Nanoscale*, 2013, **5**, 3030–3036.
20 W. Qin, D. Zhang, D. Zhao, L. Wanga and K. Zhenga, *Chem. Commun.*, 2010, **46**, 2304–2306.
21 H. Qiu, G. Chen, R. Fan, L. Yang, C. Liu, S. Hao, M. J. Sailor, H. Ågren, C. Yang and P. N. Prasad, *Nanoscale*, 2014, **6**, 753–757.
22 Y. J. Xu, J. Lin, Y. Lu, S. L. Zhong, L. Wang, L. Dong, Y. D. Wu, J. Peng, L. Zhang, X. F. Pan, W. Zhou, Y. Zhao, L. P. Wen and S. H. Yu, *Nanoscale*, 2016, **8**, 13399–13406.
23 Y. Zhu, W. Xu, S. Cui, M. Liu, C. Lu, H. Song and D. H. Kim, *J. Mater. Chem. C*, 2016, **4**, 331–339.
24 F. Lei, X. Zou, N. Jiang, Q. Zheng, K. H. Lam, L. Luo, Z. Ninga and D. Lin, *CrystEngComm*, 2015, **17**, 6207–6218.
25 C. Gong, Q. Li, R. Liu, Y. Hou, J. Wang, X. Dong, B. Liu, X. Yang, Z. Yao, X. Tan, D. Li, J. Liu, Z. Chen, B. Zou, T. Cui and B. Liu, *Phys. Chem. Chem. Phys.*, 2013, **15**, 19925–19931.
26 S. Sarkar and V. Mahalingam, *CrystEngComm*, 2013, **15**, 5750–5755.
27 G. Wang, W. Qin, J. Zhang, J. Zhang, C. Cao, L. Wang, G. Wei, P. Zhu and R. Kim, *J. Phys. Chem. C*, 2008, **112**, 12161–12167.
28 F. Tao, Z. Wang, L. Yao, W. Cai and X. Li, *J. Phys. Chem. C*, 2007, **111**, 3241–3245.
29 D. Li, C. Ding, G. Song, S. Lu, Z. Zhang, Y. Shi, H. Shen, Y. Zhang, H. Ouyang and H. Wang, *J. Phys. Chem. C*, 2010, **114**, 21378–21384.
30 B. Shao, Q. Zhao, N. Guo, Y. Jia, W. Lv, M. Jiao, W. Lü and H. You, *Cryst. Growth Des.*, 2013, **13**, 3582–3587.
31 X. Zhang, M. Wang and J. Ding, *RSC Adv.*, 2014, **4**, 29165–29172.
32 G. Murali, B. H. Lee, R. K. Mishra, J. M. Lee, S. H. Nam, Y. D. Suh, D. K. Lim, J. H. Lee and S. H. Lee, *J. Mater. Chem. C*, 2015, **3**, 10107–10113.
33 D. Chen, Z. Wan, Y. Zhou, X. Zhou, Y. Yu, J. Zhong, M. Ding and Z. Ji, *ACS Appl. Mater. Interfaces*, 2015, **7**, 19484–19493.
34 P. Chen, H. Jia, Z. Zhong, J. Han, Q. Guo, J. Zhou, X. Liu and J. Qiu, *J. Mater. Chem. C*, 2015, **3**, 8794–8798.
35 H. Suo, C. Guo, J. Zheng, B. Zhou, C. Ma, X. Zhao, T. Li, P. Guo and E. M. Goldys, *ACS Appl. Mater. Interfaces*, 2016, **8**, 30312–30319.
36 M. Lin, Y. Zhao, M. Liu, M. Qiu, Y. Dong, Z. Duan, Y. H. Li, B. P. Murphy, T. J. Lu and F. Xu, *J. Mater. Chem. C*, 2014, **2**, 3671–3676.
37 M. Ding, D. Chen, S. Yin, Z. Ji, J. Zhong, Y. Ni, C. Lu and Z. Xu, *Sci. Rep.*, 2015, **5**, 12745.
38 C. Li, J. Yang, Z. Quan, P. Yang, D. Kong and J. Lin, *Chem. Mater.*, 2007, **19**(20), 4933–4942.

